EFFECTS OF GAS-PHASE TURBULENCE ON THE DYNAMICS OF DEFORMABLE GAS–LIQUID INTERFACES

Youssef Elashmawi†, Leon Li, Simen Å. Ellingsen, R. Jason Hearst
Department of Energy and Process Engineering
Norwegian University of Science and Technology
Kolbjørn Hejes vei 2, 7034 Trondheim, Norway
†youssef.h.r.elashmawi@ntnu.no

Abstract

Shear-driven deformable surfaces such as wind waves are typically parameterised by the mean forcing velocity; however, we will demonstrate that the freestream turbulence (FST) present in the forcing phase also has an influence. We perform simultaneous particle image velocimetry of the forcing air-phase flow and planar laser induced fluorescence (PLIF) of the interface in the air–water facility at NTNU, which uses an active grid to vary the turbulence intensity and integral scale in each phase separately. We analyse the boundary layer growing above the liquid interface and how it interacts with the deformable interface. The near interface shear stress scales with the introduction of FST. The amplification of streamwise and vertical momentum transport near the interface scales in a non-monotonic fashion with increasing FST. These results clarify how turbulence modulates interface behaviour and provide insight into the underlying mechanism responsible for this modulation. This surface response phenomenon is governed by a scale-matching mechanism, whereby the energy transfer between the flow field and the interface depends on the scale separation between the turbulent energy spectrum and the position of the dominant interfacial wavelength within that spectrum.

Introduction

Wall-bounded flow research has historically focused on rigid smooth or rough surfaces. Although these problems are themselves highly complex, they have provided much of the fundamental understanding of near-boundary fluid motion. Yet most of the Earth's surface is not rigid, but deformable and dynamically responsive to the flow above and beneath it, most notably in the form of the oceans. Understanding the mechanisms governing the ocean–atmosphere system therefore requires close attention to the gas–liquid (air–water) interface, which mediates momentum and gas exchange and thereby controls climate-relevant fluxes (Jähne & Haußecker, 1998). In multiphase flows, the interface acts as the effective mediator of energy and momentum transfer: its geometry and dynamics both reflect and influence the surrounding turbulence (Turney & Banerjee, 2013). Consequently, predictive models of multiphase momentum and scalar transfer depend on a clear understanding of how the interface deforms and adjusts under varying flow conditions.

Early studies established the classical view that mean wind shear is the primary driver of wave growth, with comparatively little emphasis placed on the role of turbulent fluctuations (Miles, 1957). More recent studies employing controlled freestream turbulence (FST) generated by static grids have largely reinforced this perspective. For example, Takagaki *et al.* (2020) showed experimentally that imposed FST had only a limited effect on wave growth, suggesting that wave development is governed predominantly by mean shear rather than by random turbulent fluctuations.

At higher wind forcing, however, coherent flow phenomena become increasingly important in regulating momentum exchange. Buckley *et al.* (2020) demonstrated that intermittent airflow separation behind steep waves generates large fluctuations in surface shear stress, revealing strong coupling between wave geometry and air-side coherent structures. Funke *et al.* (2021) further characterised such wave-coherent motions, identifying sheltering vortices and recirculation zones from high-resolution pressure measurements. With simultaneous measurement of both phases Tenhaus *et al.* (2024) showed the strong wave-coherence of the phase-averaged viscous stress, the result of intermittent sheltering, capillary waves and water-side turbulence under wave crests (Tondu *et al.*, 2025). Recent experiments have also quantified turbulence above micro-breaking waves (Do *et al.*, 2024), highlighting the importance of microscale breaking processes. More recently, Abu Rowin *et al.* (2024) showed that small-scale capillary waves play a crucial role in sustaining spanwise vorticity near the interface and in modifying momentum transport relative to canonical solid-boundary flows.

Despite these advances, many previous studies either neglect FST altogether or do not treat it as an independent control parameter, instead focusing primarily on wave-dependent processes such as airflow separation, ejections, and entrapment. As a result, there remains a gap in understanding the more realistic situation in which FST, boundary-layer development, surface deformation, and water-side motion interact simultaneously. The present study addresses this gap through experiments conducted in the air—water facility at NTNU, in which both the mean flow velocity (through the bulk Reynolds number, Re_B) and the gas-phase turbulence characteristics (through the Taylor microscale Reynolds number, Re_λ) are varied using an active grid. Our objective is to determine, in a systematic and comprehensive manner, whether and how gas-phase turbulence modifies wind-driven waves and the associated interfacial statistics.

Methodology

The experiments were performed at the Norwegian University of Science and Technology air-–water facility, whose

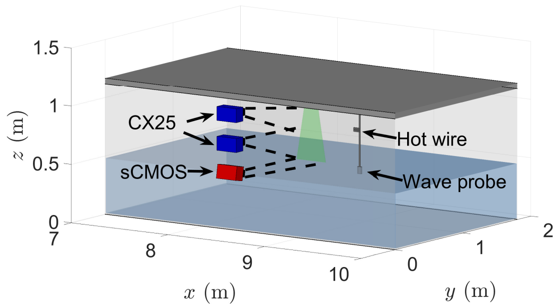

Figure 1. Experimental setup depicting the air-side acquisition. Two CX25 cameras (blue) are used for PIV and one sCMOS camera (red) is used for surface LIF.

test section measures $11.2\,\mathrm{m} \times 1.8\,\mathrm{m} \times 1.12\,\mathrm{m}$ (length (x) $\times$ width (y) $\times$ height (z)). The facility combines a recirculating open-channel flume (water phase) with an open-loop wind tunnel (air phase), enabling independent control of the mean flow in each phase. At the inlet of the test section, an active grid generates controlled turbulence in the air side, the water side, or both, permitting phase-specific prescription of turbulence statistics. By varying the rotation frequency and activation patterns of the grid bars, we tune turbulence intensity, integral length scale, and intermittency independently in air and water, thereby expanding the accessible parameter space for coupled air–water dynamics.

The 1.12 m tall test section is divided between the water and air heights, with the nominal water height maintained at 0.53 m and the air occupies 0.59 m from the still water surface to the solid wall roof of the channel, here we call this height (h). To negate direct mechanical imprinting of the grid flap movements on the free-surface, and to promote natural wave evolution, a faired wedge measuring 2.4 m long is mounted at the grid, with 2 m of the wedge extending downstream of the grid. The wedge tapers smoothly toward the free surface in both phases. At the downstream end after the test section, a porous dissipative beach suppresses wave reflection, ensuring quasi-unidirectional wave fields and clean fetch conditions.

The active grid itself is modified from Jooss *et al.* (2021) to enable independent prescriptions of different turbulence statistics in both phases. For the air phase, The horizontal bars are spun in a random mode, with central frequencies $\Omega = \{0.5, 3, 7\}$ Hz. The bandwidth of the frequency range of the grid sequences are taken to be $\omega = \pm\Omega/2$. Reference cases where the grid is kept static are also taken. The details of the cases will be explained later in this section.

All measurements are acquired at $x = 8.5$ m $85M$ downstream of the grid, where $M = 0.1$ m is the mesh length of the active grid (centre-to-centre spacing between the bars). This measurement location is chosen to ensure that the turbulence has evolved away from direct forcing, yielding approximately homogeneous and isotropic inflows for both phases. The free stream velocity characteristics are quantified with hot–wire anemometry (HWA). A Dantec 55P01 single straight wire probe is used in conjunction with a Streamline Pro anemometer. The wire has a diameter of 5 µm and a sensing length of 1.25 mm. The anemometer is set to have an internal low-pass filter at 30 kHz, while the sampling frequency is set to 75 kHz. This is more than sufficient to resolve the full air-side turbulence spectra, which have Kolmogorov frequencies around 10 kHz. Turbulence intensity (defined as $\sqrt{\langle u'^2 \rangle}/U$, hereinafter u'/U) is controlled by the active grid.

As seen in figure 1 two–dimensional, planar velocity fields in the streamwise—vertical (x–z) plane were acquired by particle image velocimetry (PIV) on the air side. The air flow is seeded using a water–based smoke fluid (JEM Pro–Fog Fluid), producing reflective droplets of nominal diameter 1 µm. Two LaVision CX 25S (25 MP) cameras provide a stitched field-of-view (FOV) of $0.20\,\mathrm{m} \times 0.55\,\mathrm{m}$ ($x \times z$). Illumination is provided by a dual-pulse Litron Nano L Nd:YAG laser with a power output of 200 mJ per pulse at 532 nm. The acquisition frequency is selected to ensure statistical independence between samples, based on the criteria of minimum of two passages of the integral length scales through the FOV between successive image pairs. The water is dosed with Rhodamine-6G dye to provide fluorescence under the illumination by the same 532 nm PIV laser; this provides line-surface measurements via laser-induced fluorescence (LIF). Surface LIF images of the dye–marked interface are acquired with a LaVision Imager sCMOS CLHS 4MP camera, and they are synchronised with the PIV acquisition. This provides a consistent, co–located record of surface deformation to pair with the velocity fields (Buckley & Veron, 2017). The effective PIV-LIF FOV is set by masking lateral margins affected by light–sheet intensity roll–off, resulting in a uniform and rectangular analysis window. Each PIV-LIF acquisition comprises of 2000 independent image pairs (single frame for LIF), under identical nominal flow settings to enable direct statistical comparison.

The processing for the velocity fields is performed in DaVis 10.2. Image pre-processing include background subtraction to remove stationary illumination patterns, frame-wise intensity normalization to mitigate low gain/illumination drift, and removal of poorly seeded frames by quality metrics on the correlation plane. Correlation is computed over four passes from $96 \times 96\,\mathrm{px}^2$ to $32 \times 32\,\mathrm{px}^2$ windows with 50% overlap, with window–deformation activated. Post–processing includes a median–test for universal outlier detection and local replacement (median interpolation) of rejected vectors. Furthermore, edge regions with light–sheet intensity roll–off are masked to maintain a uniform analysis window. The resulting velocity field has 99×609 vectors, with a vector spacing of 1 mm. To maximise near–wall fidelity, single–pixel PIV is utilised, providing sufficient spatial resolution to partially resolve the viscous sublayer (down to $z^+ \sim 6$ in inner wall units) and to extract reliable log–law mean profiles along the channel top wall (Westerweel *et al.*, 2004).

LIF images are processed in MATLAB R2023a. To suppress sensor noise while preserving capillary–scale features, a spatial sliding filter with a window smaller than the visually observed capillary wavelengths is applied. From the filtered intensity field, the magnitude of the intensity gradient $\|\nabla I\|$ is computed and supplied to an interface–tracking optimiser that enforces a smoothness/continuity constraint along the free–surface path. Starting from a physically anchored seed point at the lateral boundary, the algorithm identifies the interface as the minimum–cost (non–linear) curve that follows the high–gradient ridge of the fluorescing dye; this yields pixel–accurate interface positions frame–by–frame without the use of a global threshold. The resulting interface curve is then used to (i) co–register and crop the PIV vector fields at the air–water boundary and (ii) generate a binary time series for subsequent statistical analysis. This gradient–guided, continuity–regularised approach robustly captures both long–waves and capillary–scale features, ensuring that the full range of resolved free–surface scales is retained in the analysis.

The experimental matrix (summarised in table 1) com-

Table 1. Summary of flow statistics for the 10 test cases. Here, U_b is the air-side bulk velocity,U_∞ is the mean freestream velocity, u'/U is the turbulence intensity, Re_λ is the Taylor micro-scale Reynolds number, L_{11}/M is the integral length scale normalised by M, and η', and $\Delta\eta_{\max}$ are the interface RMS and peak-to-peak displacement, respectively.

Notation	η' (mm)	$\Delta\eta_{\max}$ (mm)	U_∞ ($\mathrm{m\,s^{-1}}$)	U_b ($\mathrm{m\,s^{-1}}$)	u'/U (%)	Re_λ (-)	$\frac{L_{11}}{M}$ (-)
S_4	1.03	4.59		3.26	2.83	119	1.53
L_4	1.95	7.88	$4 \pm 2\%$	3.34	4.61	190	1.32
M_4	1.85	7.58		3.46	4.82	213	1.36
H_4	1.40	5.96		3.33	6.04	278	2.88
S_8	4.23	15.5		6.49	4.04	226	2.28
L_8	5.11	18.4	$8 \pm 2\%$	6.59	4.85	252	1.28
M_8	5.32	19.0		6.50	5.07	266	1.37
H_8	5.24	18.8		6.64	6.52	384	3.80
S_{10}	5.28	19.0	$10 \pm 2\%$	7.47	5.29	302	2.21
H_{10}	7.27	24.8		7.83	6.91	412	4.34

prises of 10 test cases designed to separate the influences of bulk velocity and turbulence on free–surface dynamics. The parameter space spans different freestream velocities and turbulence intensities. For the 10 test cases, which consist of ten air-only, three nominal air freestream velocities, $U = \{4, 8, 10\}\,\mathrm{m\,s^{-1}}$, are chosen. The turbulence intensity ranges are $u'/U \in [1.9\%, 7.5\%]$. As a result, the interface response covered capillary–wave conditions at low relative speeds up to the onset of micro–breaking at the highest wind shear, with interface RMS (η') and peak–to–peak ($\Delta\eta_{\max}$) increasing monotonically with respect to the phase velocity difference (see table 1).

For clarity between the test case names, we adopt the following labels, I_U. Here, the subscript U denotes the nominal freestream velocity. The intensity label I denotes the FST level: S denotes static grid and it is the lowest turbulence intensity level, while L, M, H are increasing turbulence intensity. For example, L_4 is a $4\,\mathrm{m\,s^{-1}}$ run with low turbulence intensity.

Results

We begin by characterizing the incoming air–side flow at the solid wall, using inner scaling to assess whether the boundary layer is canonical. The friction velocity u_τ is estimated here using the Reynolds shear stress peak measured in the vicinity of the solid wall boundary layer, *viz.* $u_\tau \equiv [\max_z(-\overline{u'(z)w'(z)})]^{1/2}$. The resulting u_τ is then used to normalise U and z into inner wall units. Figure 2 shows the normalised boundary layer mean velocity profile, $U^+(z^+)$, for all 10 test cases. The canonical log-law is also superimposed onto the normalised profiles. The standard variables are $U^+ = U/u_\tau$, $z^+ = z u_\tau/\nu$, where $U(z)$ is the mean streamwise velocity, z is the wall–normal distance, and ν is the kinematic viscosity. For a smooth, zero–pressure–gradient turbulent boundary layer (ZPG TBL), the log layer is $U^+ = \kappa^{-1}\ln z^+ + B$, with $U^+ \approx z^+$ for $z^+ \leq 5$ (viscous sublayer).

We can see evidently that the inner–scaled profiles collapse in the viscous and logarithmic regions and align well with the canonical log-law across all cases, consistent with

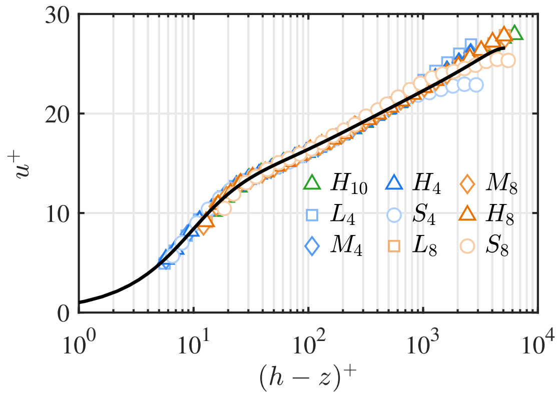

Figure 2. (Inner-scaled mean velocity profiles, plotted as U^+ versus $(h-z)^+$, where $U^+ = U/u_\tau$ and $(h-z)^+ = (h-z)u_\tau/\nu$; the use of $(h-z)^+$ preserves consistency with the co-ordinate system in which the free surface is located at $z = 0$. All cases are compared with the DNS channel-flow data of Graham *et al.* (2016) at $Re_\tau = 6000$.

previous studies (see Geva & Shemer, 2022). In the outer layer, mild departures consistent with a finite wake are observed, and modest pressure–gradient–driven variations in the wake parameter are expected (e.g. Hearst *et al.*, 2018). Within uncertainty of the fit, the wall–bounded flow thus exhibits behaviour consistent with the canonical zero-pressure-gradient turbulent boundary layer (ZPG-TBL) in the inner region across all velocity groups.

This provides a well–characterised wall reference against which we interpret the near–interface dynamics. While inner–region agreement with the log-law does not *alone* preclude interactions between the wall and the free surface, it indicates that the wall layer itself is not anomalous under our operating conditions. In the sections that follow, we proceed to assess the interplay between FST and surface layer processes using independent diagnostics (e.g. the location of the inter–boundary–layer velocity maximum, surface layer thickness/steepness measures, and shear–stress profiles), and highlight the differences against the canonical ZPG-TBL.

In figure 3, we present the normalised streamwise mean velocity profiles across the entire FOV where the velocity U is normalised by the bulk velocity calculated as $U_b = \frac{1}{h}\int_0^h U(z)\mathrm{d}z$;. The near–wall mean profiles respond systematically to increasing FST. The static–grid baseline, S_4, exhibits a relatively thin boundary layer with strong shear confined close to the wall and a rapid approach to U_∞. Introducing FST via the active grid enhances outer layer mixing and entrainment, transporting high momentum fluid toward the wall (and low momentum fluid away from it), which thickens the boundary layer and redistributes the shear across a larger portion of the profile. As a result, the mean gradient near the wall is smoother and the profile approaches the mean freestream velocity U_∞ more gradually (a “fuller” outer profile). In outer scaling, they display a wake–like shift consistent with increased turbulent entrainment. These qualitative trends are robust and repeatable across all bulk velocity groups.

In contrast to the solid–wall case, the mean profiles in the vicinity of the water surface exhibit the *opposite* trend. Introducing FST compresses the surface boundary layer: enhanced outer–layer mixing disrupts the near–surface production region, redistributes shear away from the classical surface–layer structure, and the profile reaches its outer veloc-

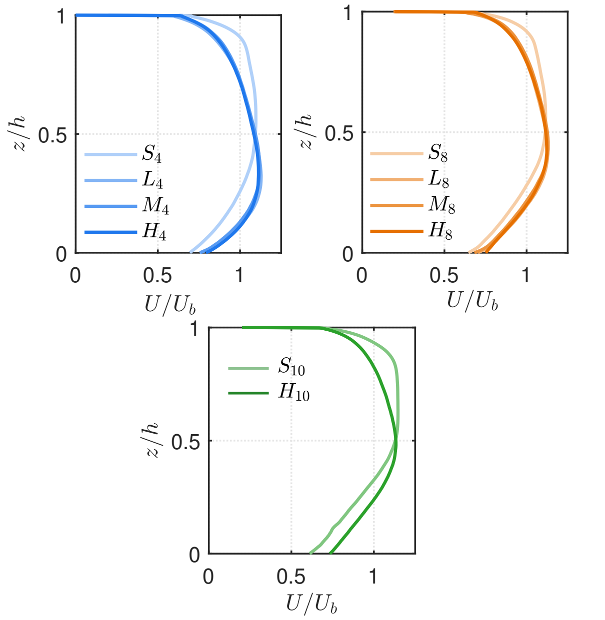

Figure 3. Normalised mean streamwise velocity profiles U/U_b versus normalised wall-normal coordinate z/h (zero at the free surface). Panels correspond to the low, medium, and high velocity cases, respectively. Within each group, shade intensity increases with Re_λ from S^4 to H^{10}. Velocity is normalised by the bulk speed U_b computed from the corresponding mean profile; height is normalised by the air-side height h.

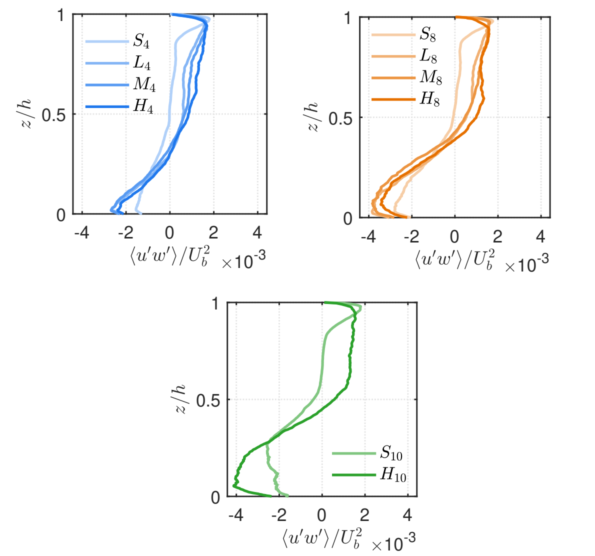

Figure 4. Normalised Reynolds shear stress profiles $\langle u'w' \rangle / U_b^2$ versus normalised wall-normal coordinate z/h (zero at the free surface). Panels correspond to the low, medium, and high velocity cases, respectively. Within each group, shade intensity increases with Re_λ from S^4 to H^{10}. Velocity is normalised by the bulk speed U_b computed from the corresponding mean profile; height is normalised by the air-side height h.

ity more rapidly. A salient indicator is the position of the velocity maximum that forms between the wall and surface layer; this maximum shifts monotonically *toward* the water surface as FST is introduced, consistent with a thinning (compression) of the surface layer. We interpret this systematic shift as evidence of competition between wall–driven and surface–driven dynamics. FST augments outer–layer entrainment and wave–coherent motions near the interface, which suppresses surface–layer growth relative to the static grid baseline. These behaviours are repeatable across all bulk–velocity groups. The behaviour observed here supports previous findings, where the dynamics at the WSBL are markedly different and become modulated by the effective roughness and phase induced by the free surface (Sullivan & McWilliams, 2010; Do *et al.*, 2024)

To probe how FST modifies momentum transfer at the water surface, we examine the Reynolds shear stress profiles and estimate the air–side friction velocity directly from the peak of the Reynolds shear stress profile in the immediate vicinity of the interface. The shear stress profiles, shown in figure 4, exhibit distinct near–surface peaks on the air side. These peaks are substantially larger than the near–wall peaks at the solid boundary, reflecting stronger vertical exchange associated with wave–coherent motions and interfacial shear. As the bulk Reynolds number increases, the wall–side profiles collapse in the inner region (classical behaviour), whereas near the free surface, the magnitude of $\langle u'w' \rangle$ increases with mean velocity and non-monotonically with FST.

FST modifies these trends asymmetrically across the two boundaries. Relative to the static grid reference, introducing FST produces (i) a pronounced increase in the interfacial peak and thus a larger u_τ very close to the surface, but (ii) a more rapid decay of $\langle u'w' \rangle$ with distance from the interface, indicating shallow penetration of the enhanced momentum transfer. Within the FST family itself (experimental cases denoted L→M→H), we observe a mild damping of the near–surface peak and of the entire profile up to the location of the inter–boundary–layer velocity maximum aforementioned. Beyond that location, the ordering reverses and the most turbulent case carries the largest shear all the way toward the wall.

These patterns are consistent with FST (and the coupled wave–coherent motions) intensifying the local interfacial momentum exchange, raising $\langle u'w' \rangle$ while concurrently enhancing outer–layer mixing that redistributes shear and accelerates its decay away from the surface. In contrast, at the solid wall, FST spreads shear over a thicker region and diminishes the sharpness of the wall peak. The differing responses at the two boundaries underscore that surface–layer dynamics under wind forcing are not a mirror image of wall–bounded behaviour, but that the response of the momentum exchange dynamics to FST is remarkably different. We hypothesise it is due to a coupled non-linear relation between the surface boundary layer and FST, which is examined through the use of spatial correlations of eddies near the water surface.

To explore how air-side eddies imprint on, and are in turn modified by, the deformable water surface, we employ a two-point spatial correlation of the streamwise velocity fluctuations. From the full PIV field, we select a reference point on the centreline at position (x_0, z_0) and compute:

$$C_r(x_0, z_0) = \frac{\langle u'(x_0, z_0)\, u'(x_0 + r_x, z_0 + r_z) \rangle}{\sqrt{\langle u'^2(x_0, z_0) \rangle \, \langle u'^2(x_0 + r_x, z_0 + r_z) \rangle}}, \quad (1)$$

where $u'(x_0, z_0)$ is the streamwise velocity fluctuations at the reference location (x_0, z_0), and $u'(x_0 + r_x, z_0 + r_z)$ denotes the streamwise velocity fluctuations at position $(x_0 + r_x, z_0 + r_z)$. This metric reveals the degree of correlation and sign change of turbulent structures through the air column, from the solid

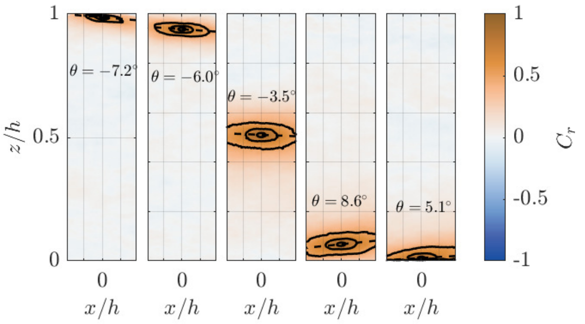

Figure 5. Streamwise velocity spatial fluctuations correlation field from boundary to boundary on the airside for the S_4 case.

wall down to the free surface.

Figure 5 shows this two-point correlation map for case S_4 for five different reference positions. In this low relative velocity case, the correlation contours remain remarkably similar between the wall-bounded layer and the free-surface layer. The eddy "tilt" angle θ taken as the angle between the line of strongest correlation passing through the origin with respect to the positive streamwise horizontal direction shows a marginally shallower nature at the free surface than at the wall (right and left panel of Figure 5, respectively); the central core is symmetric and isotropic, with a very weak signal of the influence of the wall boundary layer as it still maintains an angle away from the top wall. Near the water surface, the eddies become more elongated in the streamwise direction relative to the solid-wall. As the eddies approach the interface, wall-normal motions are increasingly constrained, which alters the Reynolds-stress anisotropy and favors elongated motions parallel to the interface, particularly in the streamwise direction. Subsequently, we will fix the reference position (x_0, z_0) close to the interface to focus on the interplays there.

Shifting our attention to figure 6, under air-only forcing at the same bulk velocity but different FST, the effect of FST on the spatial correlation, C_r, is clear. At low turbulence intensity, C_r forms a compact, positively correlated region anchored at the water surface boundary layer (WSBL) that decays smoothly toward the freestream. As FST increases, a pronounced anti-correlated ($C_r < 0$) band emerges outside the WSBL. Notably, the zero crossing of C_r collocates with the sign change in the Reynolds shear stress $\langle u'w' \rangle$ (figure 4) and with the mean-velocity peak location (figure 3). These trends indicate that increasing FST acts in a manner that connects the WSBL more with the rest of the flow field. It enhances its momentum exchange with the interface as we see from the Reynolds shear stress $\langle u'w' \rangle$ (figure 4) and allows stronger communication between the WSBL and the rest of the flow.

Discussions and implications

A solid wall imposes the classical constraints of no slip and impermeability, such that the velocity vanishes at the boundary and turbulent production is anchored directly at the wall before spreading outward into the flow. An air–water interface, by contrast, presents a fundamentally different dynamical environment. To leading order, the boundary is shear-transmitting and deformable rather than rigid. The tangential velocity at the interface remains non-zero, the tangential stress must remain continuous across the two phases, and the interface itself can deform and recover under the competing effects of gravity and capillarity. These boundary conditions profoundly alter the structure of the near-surface turbulence. In particular, vertical motions approaching the interface are suppressed, while turbulent energy is preferentially redistributed into the horizontal directions. The air-side production mechanisms near the interface are therefore expected to differ fundamentally from those over a solid boundary.

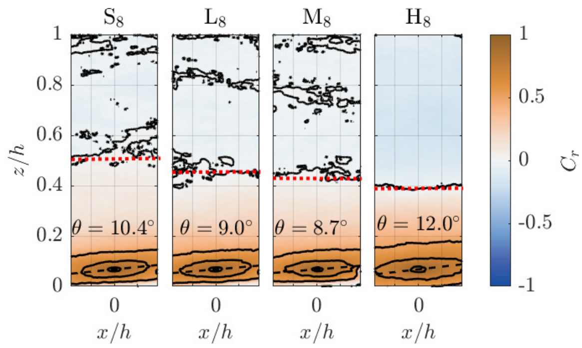

Figure 6. Streamwise velocity spatial fluctuations correlation field from boundary to boundary for turbulence settings S, L, M, H. the near surface eddy correlation panel is the only one being depicted in the 4 panels, the red dotted line indicates the zero crossing for the shear stress profile across each case.

Table 2. Measured quantities for 4 representative test cases; u_τ is the air-side friction velocity, L_{11} the integral length scale, ℓ_K the Kolmogorov length scale, and Re_λ the Taylor microscale Reynolds Number

Case	Re_λ	L_{11} (mm)	ℓ_K (mm)	L_{11}/ℓ_K	u_τ (m s^{-1})
S_8	226	228	0.383	594	0.455
L_8	253	128	0.313	408	0.531
M_8	266	137	0.309	443	0.529
H_8	384	380	0.289	1316	0.525

To attempt to rationalise the observed mechanism, one might invoke an energy-efficiency or scale-matching argument. From table 2, the first-order effect of introducing FST is clear: the turbulent energy input is consistently higher than in the static-grid case. This explains why the FST cases systematically exhibit an enhanced u_τ relative to their static-grid counterpart. Within the FST family itself, however, the response is not governed solely by the total amount of energy injected into the airflow, but by how efficiently that energy is transferred to the deformable interface.

The indication is that the air-to-water energy transfer efficiency depends on the degree of spectral scale matching between the incoming turbulence and the interface response. By contrast, when the energetic part of the turbulence spectrum is distributed farther from the dominant interfacial scale, the coupling is weaker and the momentum-transfer response is reduced, corresponding to an effective surface drag coefficient that depends not only on the mean velocity of the wind, but also the turbulent kinetic energy it carries and its spectral distribution. This notion is reminiscent of the classical theory of Phillips (1957) which ascribes early growth of wind waves to a resonance between turbulent pressure fluctuations matching the wavelength and speed of the developing wave, but as commented by e.g. Li & Shen (2022), the intensity of turbulent pressure fluctuations exerted on the water surface is usually low, and thus, the Phillips theory is commonly believed to dominate wave evolution only in the early development of wind waves.' We conjecture that a higher presence of strong turbulence at relatively low wind speeds overlapping spectrally with surface deformations could maintain the importance of a Phillips-like mechanism beyond the principal stage, which if so could increase the amplitude of small waves, thereby increasing the surface roughness and promote higher u_τ. The relation with the wave-turbulence coherent effects found by Tenhaus *et al.* (2024) and Tondu *et al.* (2025) remains a potentially key question. The range of length scales from η' to L_{11} is more than doubled between (L_4) and (H_4) (see table 2), and a scale-matching hypothesis would imply that some, but not all of the energy being injected to the interface corresponds to scales that are effective in exciting the surface state.

Conclusions

Over a wavy interface, the total air–water momentum transfer is not carried by turbulent and viscous shear alone. Rather, it partitions between (i) viscous/turbulent shear stress and (ii) pressure-induced form drag arising from the wave geometry and the associated wave-coherent airflow response, including sheltering and separation effects (Kudryavtsev *et al.*, 2014). The presence of FST modifies both channels simultaneously. On the one hand, it enhances intermittency in the near-interface region, strengthening localised shear events and increasing the unsteadiness of the surface-coupled turbulence. On the other hand, it reorganises the wave field itself by altering the scale content, slope distribution, and coherence of the interface deformation. The WSBL therefore experiences a momentum-flux balance that is qualitatively different from that of a rigid-wall boundary layer, because the turbulence is coupled not only to mean shear but also to a deformable, dynamically active boundary.

This distinction is reflected directly in the measured stress structure. The observed near-surface shear-stress peak, displaced slightly away from the interface, suggests that the strongest momentum exchange does not occur exactly at the surface but within a thin adjacent layer where wave-coherent motions, intermittent shear, and turbulent fluctuations interact most strongly. Beyond this peak, however, the stress decays rapidly with increasing distance from the interface. This rapid decay is opposite to the more familiar solid-wall response to FST, where turbulence generated near the wall tends to spread farther into the outer flow, broadening the weak shear-affected. Here, instead, FST sharpens the localization of momentum exchange near the deformable surface and causes a rapid decay of the shear into the outer air region. This behaviour indicates that the interface acts not as a passive analog of a wall, but as a selective filter that absorbs, redirects, and correlates turbulent motions according to the interfacial dynamics. The multi-point correlation maps provide particularly strong evidence for this change. When FST is present, a pronounced anti-correlation band appears just above the WSBL, and the zero-crossing aligns closely with both the location of the inter-boundary-layer velocity maximum and the sign reversal in Reynolds shear stress. This is a highly structured signature, not a random statistical artefact. The interface-linked motions remain organised around the local wave dynamics, and they are enhanced through preferential paths when the scales injected from the freestream align with the wave lengths of the interfacial deformations.

Acknowledgements

Funded by European Union (ERC, GLITR, 101041000). Views and opinions expressed are those of the authors only and do not necessarily reflect those of the European Union or the European Research Council. Neither the European Union nor the granting authority can be held responsible for them.

REFERENCES

Abu Rowin, W., Kevin, Bhirawa, T., Lee, W. J.H., Philip, J., Marusic, I. & Monty, J. 2024 High-resolution PIV measurement over wind-generated waves. *Exp. Fluids* **65**, 77.

Buckley, M. P. & Veron, F. 2017 Airflow measurements at a wavy air–water interface using PIV and LIF. *Exp. Fluids* **58**, 161.

Buckley, M. P., Veron, F. & Yousefi, K. 2020 Surface viscous stress over wind-driven waves with intermittent airflow separation. *J. Fluid Mech.* **905**, A31.

Do, J.T., Wang, B.B. & Chang, K.A. 2024 Turbulence over young wind waves dominated by capillaries and microbreakers. *J. Fluid Mech.* **985**, A22.

Funke, C. S., Buckley, M. P., Schultze, L. K. P., Veron, F., Timmermans, M.L. E. & Carpenter, J. R. 2021 Pressure fields in the airflow over wind-generated surface waves. *J. Phys. Oceanogr.* **51**, 3449–3460.

Geva, M. & Shemer, L. 2022 Wall similarity in turbulent boundary layers over wind waves. *J. Fluid Mech.* **935**.

Graham, J., Kanov, K., Yang, X. I. A., Lee, M., Malaya, N., Lalescu, C. C., Burns, R., Eyink, G., Szalay, A., Moser, R. D. & Meneveau, C. 2016 A web services accessible database of turbulent channel flow and its use for testing a new integral wall model for LES. *J. Turb.* **17**, 181–215.

Hearst, R. J., Dogan, E. & Ganapathisubramani, B. 2018 Robust features of a turbulent boundary layer subjected to high-intensity free-stream turbulence. *J. Fluid Mech.* **851**, 416–435.

Jähne, B. & Haußecker, H. 1998 Air–water gas exchange. *Annu. Rev. Fluid Mech.* **30**, 443–468.

Jooss, Y., Li, L., Bracchi, T. & Hearst, R. J. 2021 Spatial development of a turbulent boundary layer subjected to freestream turbulence. *J. Fluid Mech.* **911**, A4.

Kudryavtsev, V., Chapron, B. & Makin, V. 2014 Impact of wind waves on the air–sea fluxes: A coupled model. *J. of Geophys. Research: Oceans* **119** (2), 1217–1236.

Li, T. & Shen, L. 2022 The principal stage in wind-wave generation. *J. Fluid Mech.* **934**, A41.

Miles, J. W. 1957 On the generation of surface waves by shear flows. *J. Fluid Mech.* **3**, 185.

Phillips, O. M. 1957 On the generation of waves by turbulent wind. *J. Fluid Mech.* **2** (05).

Sullivan, Peter P. & McWilliams, James C. 2010 Dynamics of winds and currents coupled to surface waves. *Annu. Rev. Fluid Mech.* **42**, 19–42.

Takagaki, N., Suzuki, N., Takahata, S. & Kumamaru, H. 2020 Effects of air-side freestream turbulence on the development of air–liquid surface waves. *Exp. Fluids* **61**, 136.

Tenhaus, J., Buckley, M. P., Matt, S. & Savelyev, I. B. 2024 Viscous and turbulent stress measurements above and below laboratory wind waves. *Exp. Fluids* **65** (12).

Tondu, C., Gade, M., Morales Meabe, J. & Buckley, M. P. 2025 Wide-field-of-view PIV measurements above and below microscale breaking waves. *Exp. Fluids* **66** (11).

Turney, D. E. & Banerjee, S. 2013 Air-–water gas transfer and near-surface motions. *J. Fluid Mech.* **733**, 588–624.

Westerweel, J., Geelhoed, P. F. & Lindken, R. 2004 Single-pixel resolution ensemble correlation for micro-PIV applications. *Exp. Fluids* **37**, 375–384.